

The Aerosol Limb Imager: Acousto-Optic Imaging of Limb Scattered Sunlight for Stratospheric Aerosol Profiling

B.J. Elash¹, A.E. Bourassa¹, P.R. Loewen¹, N.D. Lloyd¹, D.A. Degenstein¹

[1]{Institute of Space and Atmospheric Studies, Saskatchewan, Canada}

Correspondence to: B. J. Elash (Brenden.elash@usask.ca)

Abstract

The Aerosol Limb Imager (ALI) is an optical remote sensing instrument designed to image scattered sunlight from the atmospheric limb. These measurements are used to retrieve spatially resolved information of the stratospheric aerosol distribution, including spectral extinction coefficient and particle size. Here we present the design, development and test results of an ALI prototype instrument. The long term goal of this work is the eventual realization of ALI on a satellite platform in low earth orbit, where it can provide high spatial resolution observations, both in the vertical and cross-track. The instrument design uses a large aperture Acousto-Optic Tunable Filter (AOTF) to image the sunlit stratospheric limb in a selectable narrow wavelength band ranging from the visible to the near infrared. The ALI prototype was tested on a stratospheric balloon flight from the Canadian Space Agency (CSA) launch facility in Timmins, Canada, in September, 2014. Preliminary analysis of the hyperspectral images indicate that the radiance measurements are of high quality, and we have used these to retrieve vertical profiles of stratospheric aerosol extinction coefficient from 650-1000 nm, along with one moment of the particle size distribution. Those preliminary results are promising and development of a satellite prototype of ALI within the Canadian Space Agency is ongoing.

1 Introduction

Stratospheric aerosol plays an important role in the global radiative forcing balance by scattering solar irradiation and causing an overall cooling effect that depends on the particle size distribution and the concentration (Kiehl and Briegleb, 1993; Stocker et al., 2013). These climate effects are an important and recent focus of research due to the potential contribution

1 of stratospheric aerosol to the so-called global warming hiatus (Solomon et al., 2011; Haywood
2 et al., 2014; Fyfe et al., 2013), and efforts to quantify the variability and trends in the global
3 stratospheric aerosol load are underway with various ground based and satellite data sets
4 (Rieger et al., 2015; Ridley et al., 2014).

5 Since its discovery with stratospheric balloon observations (Junge et al., 1961), stratospheric
6 aerosol has been measured with various techniques, although due to the variability of physical
7 composition and particle size, the observations are essentially always limited to some degree.
8 In-situ balloon observations continue to be used and have provided highly valuable data sets,
9 including most notably the long time series of optical particle counter measurements from
10 Laramie, WY (Deshler et al., 2003; 2006; Kovilakam et al., 2015). Aircraft-borne
11 nephelometers (Beuttell and Brewer, 1949; Charlson et al., 1969); acquire detailed in-situ
12 measurements, providing, for example, plume composition (Murphy et al., 2014), but are
13 spatially limited to the aircraft track. Ground based lidars have been used to do detailed studies
14 of the extent of volcanic aerosol plumes (Chazette et al., 1995; Sawamura et al., 2012) and
15 provide valuable insight into long term local variability and trends in the aerosol layer. For
16 example, lidar observations were used by Hofmann et al. (2009) to first report the observed
17 increase in stratospheric aerosol over approximately the last decade. However, the global
18 distribution, which can only really be obtained with satellite observations, provides invaluable
19 insight into aerosol processes and variability. A good example of this is the use of satellite
20 observations by Vernier et al. (2011b) to determine that the increased stratospheric aerosol load
21 reported by Hofmann et al. (2009) was in fact due to a series of relatively minor, mostly tropical,
22 volcanic eruptions.

23 Satellite instrumentation capable of remote sensing stratospheric aerosol has been in use since
24 the 1970's, beginning with limb sounding solar occultation measurements. These have
25 provided a reliable, accurate and essentially continuous long term record of vertically resolved
26 aerosol extinction coefficient measurements, mostly from the series of Stratospheric Aerosol
27 and Gas Experiment (SAGE) instruments (Russell and McCormick, 1989; Thomason and Taha,
28 2003). These SAGE measurements, which have a vertical resolution of approximately 1 km,
29 have generally compared well with ground based and in-situ measurements, although there are
30 challenges associated with comparing the retrieved extinction profiles to other microphysical
31 parameters (Russell and McCormick, 1989; Kovilakam et al., 2015). However, solar
32 occultation is generally a robust and stable technique as it directly measures atmospheric optical

1 depth, along with the exo-atmospheric solar spectrum with each scan, allowing for straight
2 forward retrieval of aerosol extinction coefficient (Damadeo et al, 2013). Although the
3 currently operational MAESTRO and ACE-Imager instruments on SciSat (McElroy et al.,
4 2007; Gilbert et al., 2007) have had some success producing stratospheric aerosol extinction
5 products (Vanhellemont et al., 2008; Sioris et al., 2010), the era of solar occultation
6 measurements essentially came to an end with SAGE III in 2006. However, a manifestation of
7 SAGE III is planned for deployment on the International Space Station in 2016 (Cisewski et
8 al., 2014).

9 More recently, limb scattered sunlight measurements have been used for stratospheric aerosol
10 retrievals. Although this technique has the advantage of being able to sample the atmosphere
11 throughout the sunlit hemisphere, it requires the use of a complex forward model of multiple
12 scattering processes along with at least some *a priori* knowledge of the aerosol scattering cross
13 section in order to retrieve the extinction coefficient profile. The Optical Spectrograph and
14 InfraRed Imaging System (OSIRIS) instrument (Llewellyn et al., 2004), which was launched
15 in 2001 and is presently still operational, was the first limb scatter instrument to retrieve
16 stratospheric aerosol extinction (Bourassa et al., 2007). The current OSIRIS version 5.07 data
17 product, which provides 750 nm extinction profiles at approximately 2 km vertical resolution,
18 has been shown to agree relatively well with SAGE II and SAGE III occultation measurements
19 (Bourassa et al., 2012b; Rieger et al., 2015). The SCanning Imaging Absorption spectroMeter
20 for Atmospheric CHartography (SCIAMACHY) instrument on Envisat (Bovensmann et al.,
21 1999) uses a retrieval technique essentially similar to OSIRIS to retrieve aerosol profiles at 750
22 nm with approximately 3 km vertical resolution (Ernst et al., 2012; von Savigny et al., 2015)
23 from scattered sunlight spectra. SCIAMACHY observations ceased with the demise of Envisat
24 in 2012 and although OSIRIS continues to operate, it is now in the fourteenth year of a mission
25 designed for two years.

26 The most recently launched limb scatter instrument is the Ozone Mapping Profiler Suite Limb
27 Profiler (OMPS-LP) on the Suomi-NPP satellite. Although similar in spectral range and
28 vertical resolution to OSIRIS, OMPS-LP is an imaging spectrometer that vertically images the
29 limb in a single measurement. Both OSIRIS and SCIAMACHY are grating spectrometers with
30 a narrow field of view, such that limb profiles are obtained by vertically scanning through a
31 range of tangent altitudes. The imaging capability of OMPS provides a decrease in the time
32 required to obtain a limb profile and so increases the along track sampling. Recent work on the

1 feasibility of aerosol retrieval from OMPS-LP measurements show promising results (Rault
2 and Loughman, 2013).

3 Several recent studies have highlighted the requirement for continued global stratospheric
4 aerosol observations, and especially the need to resolve, both vertically and horizontally,
5 aerosol in the lowermost stratosphere and the upper troposphere. This is the case for tracking
6 the evolution of aerosol from volcanic eruptions, which can have a substantial effect on the
7 aerosol optical depth in the lowermost stratosphere (Ridley et al., 2014; Andersson et al., 2015).
8 Furthering the understanding of the transport of aerosol near and across the tropopause would
9 also benefit from higher spatial and temporal resolution observations. This is evident in the
10 case of volcanic plumes, such as that from Nabro in 2011, the transport and origin of which has
11 been studied extensively and somewhat controversially (Bourassa et al., 2012; 2013; Vernier et
12 al., 2013; Fromm et al., 2013; Fairlie et al., 2014; Clarisse et al., 2014; Fromm et al., 2014).
13 However, this is also the case for the formation of background-level aerosol, particularly in the
14 region of the Asian and North American monsoons, which have been identified as a source of
15 substantial, seasonal and highly structured aerosol formation from precursor, tropospheric
16 source gases (Vernier et al., 2011a; Neely et al., 2014; Thomason and Vernier, 2013).

17 Many of the studies mentioned above have involved the use of Cloud Aerosol Lidar and
18 Infrared Pathfinder Satellite Observation (CALIPSO) space-borne lidar measurements (Winker
19 et al., 2007), which nominally measures backscatter profiles approximately every 300 m along
20 track with approximately 200 m vertical resolution. However, the stratospheric backscatter
21 signal is weak and requires averaging of only the night time measurements over several days
22 and typically 0.5 km vertically and 500 km horizontally (Vernier et al., 2011b). Additionally,
23 the uncertainty in the calibration with respect to the molecular background that is on the order
24 of the stratospheric aerosol signal leads to a potential bias in the stratospheric measurements
25 (Rogers et al., 2011). CALIPSO was launched in 2006 and although it is presently still
26 operational, it is also operating beyond its design lifetime.

27 Continued stratospheric aerosol observations from space are drastically needed though few, if
28 any, planned missions with such capability are underway. In this paper we present the design
29 and test of a prototype instrument for potential future satellite-based stratospheric aerosol
30 observation. The Aerosol Limb Imager (ALI) concept is a relatively small, low-cost, low-
31 power, passive instrument, suitable for microsatellite deployment, with the capability to provide
32 high spatial resolution measurements, both vertically and horizontally, of the visible/NIR

aerosol extinction coefficient. The basic idea is to leverage the clear advantages of the limb scatter technique as a passive, and therefore low mass and power, means to obtain daily global coverage, with a two dimensional hyperspectral imager for filling cross-track observation.

The ALI instrument concept is built around the use of an Acousto-Optic Tunable Filter (AOTF), which is a novel filtering technology that provides the ability to rapidly select the central wavelength of an image with no moving parts. These filters, which have recently been developed as large aperture, imaging quality devices, operate very efficiently in the red and near infrared spectral range, which is a well matched spectral range for limb scatter sensitivity to aerosol and cloud (Rieger et al., 2014). Additionally, the spectral bandpass of the AOTF, which is typically between 3-6 nm at these wavelengths, is very suitable for the broadband scattering characteristics of the aerosol limb signal. The two dimensional imaging nature of the design provides the capability to achieve at least sub-kilometer resolution at the tangent point, which is on the order of the scale size of the upper troposphere and lower stratosphere (UTLS) aerosol features mentioned above.

It should be noted that the basic instrument design concept of ALI is very similar to that of the Atmospheric Limb Tracker for the Investigation of the Upcoming Stratosphere (ALTIUS) (Dekemper et al., 2012), which is a Belgian instrument concept from at the Belgian Institute for Space Aeronomy (BIRA). ALTIUS is designed to measure limb scattered sunlight; however, it also has solar, stellar, and planetary occultation modes and is scientifically focused on trace gas measurements, particularly for ozone, whereas ALI is optimized for aerosol observation.

2 ALI Instrument Design

ALI is a simple optical system that images essentially a single wavelength at a time through the use of an acousto-optic tunable filter (AOTF). The AOTF is a unique device that allows for the filtering without any moving parts and relatively low power consumption. However, the AOTF operation requires important instrument design considerations to account for its optical operation. For example, the diffractive qualities of the AOTF depend on the angle that light enters the device. Additionally, in practice the AOTF output is limited to a single linear polarization, which reduces the system throughput and causes potential internal stray light in the system through the rejection of the other linear polarization. The following sections provide a brief introduction to the physical operation of the AOTF, considerations for implementation in a system designed specifically for aerosol, and an overview of the final ALI optical design.

2.1 Acousto-Optical Tunable Filter

The primary filtering device behind ALI and the technology that allows for the two dimensional spatial imaging is the AOTF, which is typically made from a birefringent crystal. A radio frequency (RF) wave is propagated through the crystal, and forms an acoustic standing wave that interacts with an incoming beam of light in an effect similar to the diffraction of a specific wavelength. The use of an AOTF for an imaging system has several distinct advantages due to its low mass, fast stabilization times of a few microseconds, and no moving parts. Although many applications use small, non-imaging AOTF's with various configurations, large aperture, birefringent, non-collinear acousto-optic devices are typically used in imaging systems. A non-collinear device is one where the input light beam and the RF acoustic wave are not aligned. Thanks to recent advancements in non-collinear AOTF technology these devices now have relatively high efficiency and robust imaging quality (Georgiev et al., 2002; Voloshinov et al., 2007).

To create the diffraction of a specific wavelength, a momentum matching criteria must be held where the wave vectors of the acoustic wave match the difference of the incoming and diffracted light wave vectors as seen in Figure 1. This condition is known as the Bragg matching criteria and is given by

$$\mathbf{k}_i = \mathbf{\kappa} + \mathbf{k}_d \quad (1)$$

where $|\mathbf{k}_i| = 2\pi n_i/\lambda$ is the wave number of the incident light, $|\mathbf{k}_d| = 2\pi n_d/\lambda$ is the wave number of the diffracted light, and $|\mathbf{\kappa}| = 2\pi F/\nu$ is the wave number of the acousto wave. The parameters λ , F and ν are the wavelength of light in vacuum, the frequency of the RF wave, and the phase velocity in the crystal respectively and the indices of refraction for the incident and diffracted light are n_i and n_d respectively. Using the condition given in Equation 1 and the wave vector diagram gives the following relation for a birefringent material undergoing Bragg diffraction

$$\lambda = \frac{\Delta n \nu \sin^2(\theta_i + \alpha)}{F \sin \theta_i} \quad (2)$$

where Δn is the absolute difference between the ordinary and extraordinary indices of refraction, θ_i is the angle of incidence of the incoming light, and α is the angle the acoustic wave propagates through the device (Voloshinov and Mosquera, 2006). Note that the wavelength diffracted by the AOTF is inversely related to frequency of the RF wave. This

equation also displays an important implication of the operation of the device that affects the design possibilities in an imaging system. That is, the wavelength of diffracted signal is dependent on the angle of incidence of the incoming wave. Therefore, passing the light beam through the AOTF at different incident angles will result in slightly different outgoing diffracted wavelengths. Also, through the described interaction, the diffracted light goes through a 90° rotation in polarization (Voloshinov, 1996).

For ALI prototyping purposes, a 10x10 mm aperture imaging quality ATOF was acquired from Brimrose of America (model number TEAFI10-0.6-1.0-MSD) with a Gooch and Housego driver (model number 64020-200-2ADMDFS-A). The AOTF is optically tuned for the wavelength octave of 600 nm to 1200 nm, corresponding to an RF range of 156 to 70 MHz. It is made from tellurium dioxide (TeO₂), a birefringent crystal with indices of refraction at 800 nm of 2.226 and 2.373 for the ordinary and extraordinary modes respectively (Uchida, 1971). The acousto-optic diffraction angle is not constant angle with wavelength, so in order to achieve an essentially constant diffraction angle the rear surface of the crystal is cut at a specific angle, such that the refraction at this final surface compensates for the angular change with wavelength. For our specific sample, the diffracted extraordinary light beam is compensated in this way and is diffracted 2.7 degrees from the input optical axis of the device. The ordinary light beam also undergoes diffraction, but at a non-constant angle from the optical axis with respect to wavelength and is not imaged by the system. A schematic of the basic light paths through the AOTF is shown in Figure 2a.

2.2 Instrument Design

The ALI prototype that we have developed has been designed specifically for testing from a stratospheric balloon at a float altitude of approximately 35 km. In this geometry, a field of view that captures a vertical image of the limb from the horizontal at float down to the tangent line to the surface corresponds to 6 degrees (Figure 3). This is substantially larger than similar imaging requirements from low earth orbit, where the same tangent altitude range would be covered by about a one degree field of view. The target vertical resolution of the measured radiance profiles is 200 m in tangent altitude. A wavelength range of 600-1000 nm was decided upon for the prototype, mostly to align well with the spectral response of a standard and readily available CCD detector. We also attempted to pay careful attention to stray light reduction including both internal scatter and out-of-field signal.

1 The use of the AOTF essentially limits the optical design to two possible basic layouts: the
2 telecentric or the telescopic system. This limitation is mainly that the incoming light beams at
3 the AOTF device must enter at less than the acceptance angle, which is defined by a threshold
4 beyond which the diffraction efficiency falls off sharply. These AOTF layouts have been
5 studied previously (Suhre et al., 2004); however they are briefly explained here in the context
6 of our intended purpose of limb imaging aerosol. The upshot is that the telescopic, or afocal,
7 system causes a wavelength gradient to be formed across the image plane, whereas the
8 telecentric design overcomes this problem but has a larger spectral point spread function, and a
9 slight change in focus with wavelength. The optical design software Code V was used to assist
10 in designing and analyzing the performance of both of the optical layouts.

11 A telecentric layout leads to focused light bundles passing through the AOTF. The filtered
12 image then has a constant wavelength across the entire image with a larger spectral point spread
13 function, since the diffracted wavelength is dependent on incident angle, as seen in Equation 2.
14 This layout has two inherent issues. First, it is sensitive to any surface defects of the crystal
15 since the light path is focused very near the AOTF surfaces. Second, a shift in the location of
16 the imaging focal plane occurs that is dependent on wavelength such that perfect focus can only
17 be obtained for a single wavelength. Defocusing will occur at the image plane for all other
18 wavelengths and in order to correct for this problem additional compensating optics would need
19 to be added or the detector would need to be actively moved as the wavelengths are scanned.

20 In the telescopic layout, collimated light for each line-of-sight passes through the AOTF. This
21 results in a few fundamental differences that both improve and degrade the imaging quality.
22 First, the light passing through the AOTF from a single line-of-sight enters the AOTF at the
23 same angle, so the image will have a narrower spectral point spread function than the telecentric
24 counterpart. However, each line-of-sight will be diffracted with a different fundamental central
25 wavelength due to the angular dependence in the AOTF diffraction (Equation 2). The scanned
26 spectrum then has better spectral resolution than obtained with the telecentric system, but there
27 will be a wavelength gradient radiating out from the center of the image. Second, since light in
28 this design passes through the AOTF collimated, the focal point of the image no longer changes
29 with wavelength. Instead, a lateral displacement of each line-of-sight occurs based on the angle
30 of incidence and the diffracted wavelength which causes a slight change in magnification of the
31 final image. The lateral displacement that occurs is given by the following relation

$$\delta = (n(\lambda) - 1) \frac{t\theta}{n(\lambda)} \quad (3)$$

where δ is the displacement from the original path. However, it turns out that this wavelength dependant change is negligible for the current ALI design.

In light of the requirements for imaging aerosol, we have chosen a telescopic design for the ALI prototype. Since the wavelength gradient across the image is small compared to the slowly varying aerosol scattering cross section, the fixed image plane is preferable for the improvement it provides in spatial imaging, particularly as we desired to use as simple as possible an optical design.

We used a very simple three lens optical layout with commercial off-the-shelf components. Two lenses before the AOTF form a simple telescope for the Front End Optics (FEO), and a single focusing lens behind the AOTF comprises the Back End Optics (BEO). The AOTF is oriented such that the detected image is formed from the diffracted beam of the vertically polarized, i.e. extraordinary, light (defined at the entrance aperture). A linear polarizer with an extinction ratio greater than 10^{-5} is placed at the back of the FEO to remove the incoming horizontal, or ordinary, polarized beam. The diffracted extraordinary beam undergoes a 90° rotation in polarization so a second linear polarizer, oriented at 90° to the first, is used after the AOTF and before the BEO to remove the undiffracted beam. This is shown schematically in Figure 2b. Note that even with the high extinction ratio of the polarizers, a not insignificant fraction of light that is intended to be blocked passes through the system. The diffracted extraordinary signal compresses at most a ~ 10 nm bandpass fraction of one polarization such that the unabsorbed broadband signal from the polarizers can be on the same order of intensity as the diffracted signal.

The extraordinary diffracted light is 2.7° from the optical axis and to compensate, the entire optical chain after the AOTF is mechanically aligned with this direction. The BEO forms the image of the signal on a QSI 616s 16 bit CCD with 1536 by 1024 pixels. A ray tracing diagram for ALI's optical system was created using the CODE V optical design software and can be seen in Figure 4. No corrections were attempted to reduce chromatic or spherical aberrations within the system and the system exhibits some coma due the large field of view and the curvature of the lenses near the edge of the field of view. Analysis with Code V shows that the distortion due to these effects across the center two degrees of the field of view is a change of less than 1% change across the entire wavelength range. The final one degree shows a distortion

1 of less than 4%. An analysis was also performed to determine the minimum resolution required
2 to achieve a Modular Transfer Function (MTF) of 0.3 across the entire field of view for all
3 wavelengths (Smith, 2000). To obtain the MTF across the entire field of view a 7 pixel running
4 average is required. This translates to an average vertical and horizontal resolution of 210 m
5 across the entire ALI field of view at the tangent point. A tolerance study was also performed
6 with Code V to assess the capability of the system within the tolerances of the mounting
7 equipment and was found that the system was insensitive to tilts and offsets within the system.

8 The SASKTAN-HR (Bourassa et al., 2008; Zawada et al., 2015) radiative transfer model was
9 used to assist in determining exposure times and entrance pupil of ALI. This was performed by
10 using ground-based sky measurements during a cloudless day at an azimuth of 90° from the sun
11 at a variety of exposure times (0.01 to 60 seconds) and wavelengths (600 to 1000 nm). The sky
12 measurements were used to estimate typical exposure times. The SASKTRAN-HR model was
13 used to compute the ratio of the modeled radiances from a balloon flight geometry to the
14 ground-based geometry to scale the ground-based exposure times to those for balloon flight.
15 The ALI entrance pupil was selected at 9.91 mm to yield flight exposure times on the order of
16 1 second. A summary of the optical specification for the ALI prototype is given in Table 1.

17 A long standing concern in the design of limb scatter instruments is the effective rejection of
18 out-of-field stray light. This is due to the bright surface very near to the targeted limb in
19 combination with the exponentially dropping limb signal with tangent altitude. For ALI test
20 observations from the stratospheric balloon, a front end baffle was incorporated. This was
21 designed to minimize the percentage of out-of-field light that can reach the aperture without
22 encountering at least three baffle surfaces. To further reduce the unwanted signal, each baffle
23 maintains a height to pitch ratio greater than 0.5 (Fischer et al, 2008). The baffle is 300 mm
24 long with a cross section of 70x70 mm and contains seven veins spaced throughout the length.
25 The effectiveness of the baffle was measured against that of a simple aperture through
26 laboratory testing yielding an approximately 8 fold decrease in measured out-of-field stray
27 light.

28 A SolidWorks rendition of the completed ALI prototype is shown in Figure 5. The base plate
29 of the instrument is tilted at 3° from the horizontal so the complete 6° vertical field of view
30 spans from the tangent point to the ground to the float altitude once mounted on the level balloon
31 gondola. With the simple off-the-shelf optics the operating temperature of ALI during the
32 mission was not actively controlled, although the instrument temperature is monitored in

several locations along the optical chain and at the detector for later analysis. A simple covering of insulating foam with a reflective coating was used to reduce temperature extremes due to the cold ambient environment and direct solar heating.

Software and controlling hardware for the instrument was developed for autonomous or commanded control during the balloon flight. A Debian Linux operating system with C++ based software controls the hardware and science data collection operation. The onboard computer is a VersaLogic PC-104 OCELOT computer with fanless operation and a thermal operating range of -40 to 85°C. The onboard system provides two-way communication to a ground based station through UDP protocol and sends data, including images and housekeeping information, to the ground, as well as receives commands from ground control.

It should be noted that our choice of a telescopic optical layout for ALI is actually the opposite choice of that made for the ALTIUS design, which uses a telecentric optical layout. For that instrument, the need for spectral resolution for trace gas retrieval makes the decision to use telecentric optics quite clear (Dekemper et al., 2012). Given that basic design difference, the overall optical specifications are quite similar between the ALI and ALITUS prototype instruments (again see Table 1 for ALI specifications), although two key differences are noted. First, by using a telescopic layout the maximum field of view for ALI is determined by choosing lenses to ensure light enters ALI within the acceptance angle of the AOTF. This allows for a larger possible field of view than with a telecentric system where the field view is defined by the aperture of the AOTF. Second, the f-number for ALTIUS is 14.32 compared to 7.5 for ALI, which allows ALI to increase light throughput at the cost of slightly higher aberrations in the final image. Dekemper et al. (2012) reports that the visible channel of ALTIUS was breadboarded and tested by taking ground based measurements of a smoke stack plume. They used the measurements to retrieve NO₂ slant column density using 10 second exposure times; although, they note that an increase in measurement frequency would improve the instrument capabilities. This also factored into our decision to use telescopic optics to increase throughput for ALI.

3 Calibration

A series of pre-flight laboratory calibrations were performed in two stages. First, the AOTF was characterized to calibrate it with respect to wavelength registration and spectral point spread function. Secondly, the instrument was characterized as a complete system to provide calibrated radiance. The following calibration measurements were performed on ALI:

- AOTF wavelength calibration
- AOTF point spread function and diffraction efficiency
- Stray light calibration
- Flat-fielding correction

3.1 AOTF Wavelength Calibration

The relationship between the applied acoustic wave frequency and the diffracted wavelength, which is known as the tuning curve defines the wavelength registration to the RF wave of the collected images. This was determined in the laboratory setting by filling the AOTF aperture with collimated light and observing the diffracted, or filtered, signal with a HORIBA iHR320 spectrometer and Synapse 354308 1024x256 pixel CCD. The grating used with the spectrometer had a spectral resolution of 1.2 nm, which is much less than the factory specified resolution of the ATOF. Images were taken at a constant exposure time at a set of acoustic wave radio frequencies spaced every 150 kHz from 75 MHz to 160 MHz. This corresponds to approximately one image every 1 nm. A typical spectrum recorded with the iHR320 is shown in Figure 6a. The fringes that are visible in the spectrum in Figure 6a are a known acousto-optic effect (Xu and Stroud, 1992) and for ALI amount to 8 to 14% of the total signal depending on wavelength and incident angle. The maximum value of each image is then taken to be the central wavelength at each respective acoustic wave frequency.

These central wavelengths for the full set of spectra were empirically found to follow a power function of the form

$$F = a\lambda^{b+c \log \lambda}. \quad (4)$$

The fit of the data to this function form agrees to less than 0.1% throughout the whole wavelength range such that the final tuning curve was as determined as

$$F = \exp(19.793) \lambda^{-3.381+0.168 \log \lambda} \quad (5)$$

where λ is in nanometers and F is in MHz with a 0.1% error in the central wavelength (see Figure 6b). It should be noted that even though the AOTF optical range is 600 nm to 1200 nm our analysis only measured wavelengths from 600 nm to 1080 nm due to the low quantum efficiency of the CCD beyond this range.

3.2 AOTF Point Spread Function and Diffraction Efficiency

The spectral point spread function and diffraction efficiency of the AOTF were also determined in a similar fashion. The same set of experimental data that was used for the wavelength registration was used to find the spectral point spread function by finding the full width at half maximum for each obtained spectrum. These range from 2-5 nm, increasing monotonically with wavelength, and are shown in Figure 6c. This spectral resolution is well within the specification required in order to retrieve aerosol information as the aerosol scattering cross varies relatively slowly across the visible and near infrared spectral range.

The same set of experimental data was also used to determine the diffraction efficiency of the AOTF, along with an additional measurement of the intensity of the incident collimated light beam. This was simply acquired by removing the AOTF from the same experimental setup. The incident light source was then measured with the iHR320 spectrometer and Synapse CCD. By taking the ratio of the intensity at the diffracted wavelength to the incident intensity the diffraction efficiency was determined. It was found to vary between 54-64% across the measured spectral range. It should be noted that the diffraction efficiency changes also with respect to incoming angle and this experimental determination only measured the diffraction efficiency at normal incidence (Xu and Stroud, 1992).

3.3 Stray Light

A laboratory experiment to characterize the stray light in the ALI system was also performed. Two types of stray light exist; the first is out-of-field stray light, i.e. signal that enters the optical path that originates outside of the field of view. The second is internal stray light, which is caused by scattering, reflections or other imperfections in the optical elements. As mentioned above, stray light removal is quite critical for limb scatter measurements.

The use of the AOTF has potential to increase the amount of internal stray light due to the fact that the undiffracted beam and the unmeasured polarization also propagate through the system. However, the diffraction interaction only occurs when the acoustic wave signal is applied, so without the acoustic wave the recorded measurement only contains the stray light in the system. Using this characteristic, the stray light of the system was measured in the laboratory. A 250 W quartz-tungsten light source was passed through a dispersing screen and onto the entrance aperture of ALI, effectively filling the entire aperture and all angles within the field of view. Using a variety of exposure times, ranging from 0.1 s to 60 s and wavelengths from 650 to 950

nm in 25 nm intervals, this diffuse source was imaged twice; once with the AOTF in its off state, with no driving acoustic wave, and once with the ATOF in its on state, with the acoustic wave applied (see Figure 2c). For each pair of measurements the image with the “AOTF-off” only contains stray light in the system, and the “AOTF-on” image contains the stray light combined with the image of the diffuse source. Subtracting the “AOTF-off” image from the “AOTF-on” image yields a final image that contains only the image of the diffuse source. A typical example of a resulting image is shown in Figure 7. The observed vignetting is caused by the aperture of the AOTF and is expected from the ray trace model. Note that this method also removes any dark current associated with the detector. This two-image method was used operationally during the balloon measurement campaign such that images captured had a corresponding “AOTF-off” image immediately obtained with the same exposure time.

3.4 Relative Flat Fielding Calibration

The flat-field calibration corrects optical and detector level differences in the system across the field of view such that a calibrated image of a perfectly diffuse source yields a constant value across the image. The resulting images from the diffuse source described above were used to determine the flat fielding corrections for ALI. These were determined in two steps: spatial and spectral. First, for the spatial correction, for each image at a given wavelength, each pixel was scaled to the mean value of the center 25x25 pixels, which had no more than a 4% standard deviation. ALI is most sensitive at 775 nm so this wavelength was chosen as the reference wavelength of a relative spectral calibration. All flat-fielding corrections were then scaled to the blackbody curve of a tungsten halogen bulb normalized to 775 nm assuming an operating temperature of 3300 K for the bulb using a method by Kosch et al. (2003). No absolute calibration was performed due to lack of availability of an appropriately calibrated source.

4 Stratospheric Balloon Flight

4.1 Flight Conditions and Measurement Modes

The Canadian Space Agency (CSA) balloon launch base is in Timmins, Ontario (48.47°N 81.33°W). ALI was integrated onto a CNES pointed gondola and used on-board subsystems, including communications and power. The CNES gondola is an actively pointed gondola with azimuthal pointing precision better than 1' with the use of an onboard star tracker. ALI was

orientated so it would be maintained at 90° from the azimuthal direction of the sun, with an overall southern field of view during the mission.

On September 19, 2014 at 05:35 UTC (01:35 local time) ALI was launched as part of the Nimbus 7 mission from the CSA Timmins balloon launch facility. During the launch, the sky was clear with light winds allowing for a safe and uneventful launch. The ascent of the gondola occurred in darkness and reached its flight altitude of 36.5 km at 8:17 UTC. First light was observed by ALI at 9:39 UTC and spectral images were recorded until 14:42 UTC. A visualization of the flight path with major landmarks noted can be found in Figure 8a. Temperature profiles for the ambient atmosphere and instrument are shown in Figure 8b. The black curve is the ambient atmospheric temperature at the gondola altitude and location during the flight as obtained from ECMWF reanalysis (Dee et al., 2011).

During the mission, ALI operated in two primary acquisition modes, a calibration mode and an aerosol imaging mode. The first mode, the calibration mode, was primarily used during ascent when the gondola was in the darkness and intermittently between the aerosol mode during sunlit conditions. During this mode the filtering of the AOTF was not enabled and the system imaged essentially only dark current during the ascent in darkness and stray light during sunlit conditions. Eight exposures are taken in the calibration mode with 0.05, 0.1, 0.5, 1, 2, 3, 5, 10 second exposure times. The second operational mode, the aerosol mode, recorded measurements in a cycle that contained 13 pairs of images across the spectral range (650-950 nm every 25 nm), the pairs being a calibration image with the “AOTF-off” and an image of the limb. Each cycle took approximately 12 minutes with each measurement set taking approximately 45 seconds to acquire with exposure times varying between 0.5 to 6 seconds.

4.2 Limb Measurements

After the successful post-flight recovery of ALI, 216 raw images were obtained and calibrated as detailed in Section 3. An example of a calibrated limb image is shown in Figure 9a. This is image number 208 at 750 nm taken at 13:57 UTC with a solar zenith angle and solar scattering angle of 63° and 98° respectively. The horizontal structure across the images is nicely revealed by calculating the mean radiance profile across the image and then removing it from each profile. This is shown in Figure 9b, where thin clouds (2 km vertical extent or less) are clearly seen near and below the tropopause level, with substantial variation in tangent altitude across the horizontal field of view. These clouds were also observed from other instruments on board

the gondola during the mission (B. Solheim, private communication). A brief check on the CALIPSO quick-look plots also shows clouds at a maximum height of approximately 13 km from measurements taken at 08:40 UTC at 47.24°N, 95.25°W, the nearest measurement point to the ALI location and time. Although these images only have a 35 km extent in the horizontal direction, there is also some indication of horizontal variation in radiance significantly above the cloud level, possibly due to real atmospheric variability in the aerosol layer. It should also be noted that some high altitude stray light is also visible in this mean residual image that was not observed in the laboratory tests. This may be due to contamination from scattering from a baffle vein or a nearby component of the gondola, although the true cause is unknown at this point.

For ease of further analysis, and to increase the precision of the measurements to a minimum of 0.6 MTF the images were averaged into cells of 25 pixels horizontally, and average vertically onto a 1 km tangent altitude grid. The radiance profiles from the center column of the images for all measurements obtained during the flight are shown in Figure 10. The first sets of profiles, the dashed lines, which start near zero and move toward larger values, are the measurements that were recorded near and during sunrise so the gradual increase is therefore expected. Measurements obtained for solar zenith angles less than 90° are represented by the solid lines. These radiance profiles follow a similar, and expected exponential shape, with some variability at tangent altitudes below 12 km corresponding largely to changing cloud conditions.

A full cycle of 13 spectral images (numbers 204-216) were used in Figure 11 to show the spectrum of relative calibrated radiances at selected tangent altitudes. The estimated uncertainty in the radiance is represented by the shading. The uncertainty is approximately five percent from 5 to 20 km and increases up to eight percent from 20 to 35 km. The error term includes the CCD read, DC offset, dark current, stray light removal, and flat fielding correction error terms. The spectra display the expected and relatively smooth fall off in intensity with increasing wavelength with Chappuis ozone absorption seen at the lower wavelengths; however, the reason for the peak in the spectra at 875 nm is not known and may be due to an inconsistency in the pre-flight calibration.

4.3 Retrieval Methodology

As a first application of the ALI measurements, we have applied a slightly modified version of the standard OSIRIS stratospheric aerosol extinction retrieval (Bourassa et al., 2012b) to the

flight measurements. This inversion algorithm, which is applied from the tropopause to 30 km altitude, assumes log-normally distributed hydrated sulphuric acid droplets in order to calculate the aerosol scattering cross sections from the Mie scattering solution (Wiscombe, 1980). The modeled radiances for the nonlinear inversion were computed with the SASKTRAN High Resolution radiative transfer engine (SASKTRAN-HR) (Bourassa et al., 2008; Zawada et al., 2015) using the newly developed vector module for polarization (Dueck et al., 2015). The output of SASKTRAN-HR gives the Stokes vectors for the radiance on the model reference frame, which are then rotated into the instrument's coordinate system. Once rotated, the polarization signal required to match the ALI measurement is the vertical polarization given by

$$I_v = \frac{1}{2}(I - Q) \quad (6)$$

where I and Q are Stokes parameters defined by $I = \langle E_x^2 \rangle + \langle E_y^2 \rangle$ and $Q = \langle E_x^2 \rangle - \langle E_y^2 \rangle$. The variables E_x and E_y are the horizontal and vertical component of the electric field in the instrument reference frame.

The relative radiance measurements from ALI are used to create measurement vectors, \mathbf{y} , as specified in Bourassa et al. (2012) in the form,

$$\mathbf{y} = \log\left(\frac{I_v(\mathbf{z}, \lambda)}{I_v(z_{ref}, \lambda)}\right) - \log\left(\frac{I_{v,rayleigh}(\mathbf{z}, \lambda)}{I_{v,rayleigh}(z_{ref}, \lambda)}\right) \quad (9)$$

where $I_v(\mathbf{z}, \lambda)$ is the measured relative radiance from ALI and $I_v(z_{ref}, \lambda)$ is the relative radiance at a high reference tangent altitude where there is little aerosol contribution. For the ALI measurements, the highest possible tangent altitude where the signal is above the noise threshold is approximately 30 km tangent height. The second term in Eq. 8 uses modeled radiances from SASKTRAN-HR with only the molecular atmosphere to approximately remove the Rayleigh signal. This is done to improve the speed of the convergence of the retrieval (Bourassa et al., 2012b). An initial guess state, \mathbf{x} , for the aerosol extinction and an assumed particle size distribution profile are set in the SASKTRAN-HR model. The forward model vector is then constructed similarly to the measurement vector, and used in combination with the measurement vector to update the aerosol extinction coefficient profile using Multiplicative Algebraic Reconstruction Technique (MART) algorithm,

$$x_i^{n+1} = x_i^n \sum_j \frac{y_j}{F(z_j)} W_{ij} \quad (7)$$

where x_i is the aerosol extinction at each model altitude, i and j denotes a tangent altitude from the measurements. W_{ij} is the weighting matrix that relates the importance of each element of the measurement vector to each shell altitude. This method described in detail by Bourassa et al. (2007).

Once a retrieval has been completed for a measured radiance profile, the result is then used to estimate the error in the retrieved extinction. For each altitude, a gain matrix, \mathbf{G} , is calculated through successive numerical perturbation of the measurement vector and re-retrieval (Rodgers, 2000). A much faster method to use the Jacobian to determine the error has been performed (Bourassa et al., 2012a) but makes an assumption that the gain matrix is equal to the inverse of the Jacobian, as typically the averaging kernel is close to the identity matrix. However, this method adds additional uncertainty to the error estimate and with a limited set of balloon data, it is possible to calculate the gain matrix directly. The error at each retrieved altitude is then given by

$$\mathbf{E} = \mathbf{G} \mathbf{S}_\epsilon \mathbf{G}^T \quad (8)$$

where \mathbf{S}_ϵ is the covariance matrix of the measurement vector and \mathbf{E} is the covariance of the retrieved aerosol profile (Rodgers, 2000). The reported precision for ALI aerosol extinction retrievals is the square root of the diagonal of \mathbf{E} .

Using the retrieved extinction profiles for the complete spectral range, we have attempted a determination of the Angström exponent using a method similar to that outlined by Rault and Loughman (2013) for the OMPS-LP analysis. In this method, the independently retrieved extinction profiles at each wavelength and altitude are fit with a straight line in log-wavelength, log-extinction space. The slope of this line corresponds to the Angstrom exponent. This is then used to find the best match to the spectral dependence of the Mie scattering cross section in order to update the particle size distribution. With only one piece of information, the mode-width of the log-normal distribution is fixed to 1.6 and the mode radius is updated. The extinction retrievals are then performed again at each wavelength and the process is iterated until the Angstrom exponent, corresponding to the determined mode radius, converges.

Ideally, the ALI measurements would be used independently to also retrieve ozone in the Chappuis band. However, due to the spectral range of the prototype, only a small fraction of the long wavelength side of the absorption band was captured. For this analysis, we have not retrieved the ozone profile but have set the ozone profile in SASKTRAN-HR to an average of

the five closest coincident ozone profiles measured by OSIRIS at the ALI location and time. The surface albedo used is also from the OSIRIS scans since the two instruments share a similar measurement method and should determine a similar albedo for the cloudy conditions. Preferably albedo would be determined from the ALI following the method of Bourassa et al., 2012b, however due to the lack of an absolute calibration this was not possible.

4.4 Results

The above retrieval method was applied to a complete cycle of ALI spectral images (number 204-216 of the balloon mission). The retrieved aerosol extinction profiles can be seen in the left panel of Figure 12. Note the log scale. After the retrieval, the difference between the measurement and forward model vectors were less than 2% for the majority of the retrieval region, approximately 13 km to 28 km, across all wavelengths. Note the behavior of decreasing extinction with increasing wavelength as expected due to the dependence of the cross section with respect to particle size.

The ALI 750 nm aerosol extinction profile is shown in the right panel of Figure 12 in blue with the shading representing the precision of the retrieval. The error is strictly based on measurement error and neglects any model and atmospheric state errors. The green curve is the average 750 nm aerosol extinction profiles of the same five coincident OSIRIS scans used for the ozone profile. The retrieved extinction profiles from ALI and OSIRIS are within with the total retrieval uncertainty below 20 km. It is encouraging, however, that the instruments follow the same overall profile shape including the stratospheric layer and the steep increase below 15 km. However, the OSIRIS and ALI extinctions do not agree within error between 20 to 25 km. Aerosol is notoriously difficult to validate in remote sensing with various technique and instrument geometries, and yet the SAGE II, SAGE III and OSIRIS differences are generally below 20-30% up to 30 km (Bourassa et al., 2012b; Rieger et al., 2015) so the disagreement between OSIRIS and ALI from 20 to 25 km found here is somewhat puzzling. However, given the retrieved uncertainty, the OSIRIS profile is only outside the upper error bound of ALI by less than 10%. There are also several possible systematic errors not accounted for in the inversion including the choice of retrieval altitude ranges, particle size composition and distributions, stray light, and the high altitude aerosol load. This is also the first polarized limb scatter retrieval to our knowledge and so there may be further issues to explore with the polarized measurement and forward model. Regardless, the results are encouraging.

The particle size method outlined above was also applied to this measurement set. The retrieved extinction at a given altitude was rejected from the straight line fit if the converged forward model radiance at that altitude was not within 2% of the measurement vector. In the case shown in Figure 13, at the 14.5 km altitude point, only 10 of the 13 possible wavelengths contributed to the determination of the Angström exponent. The first panel of Figure 13 shows the median Angström exponent that was determined after each iteration and convergence can be seen after a couple iterations. The results are shown in the second panel of Figure 13, where the Angström exponent is between 2 and 3 throughout the altitude range from 13 to 22 km. Assuming a mode width of 1.6 yields a median mode radius of 0.077 μm . In comparison to typical levels of background aerosol from the Laramie, Wyoming OPC data (Deshler et al., 2003) the retrieved particle size parameters are certainly within an expected range, although there is a relatively large error bar on the retrieved value, limiting the usefulness of the retrieved particle size information for background aerosol. However, with these error bars, even this limited spectral range would have the sensitivity to detected particle size changes as seen by OSIRIS and SAGE II over recent decades due to small volcanic perturbations (Rieger et al., 2014).

5 Conclusions

The ALI prototype, which is telescopic acousto-optic imager, has been used to successfully measure two dimensional spectral images of the atmospheric limb from stratospheric balloon. The observed radiances appear to be of high quality and show both vertical and horizontal features of the cloud and aerosol layers. Aerosol extinction coefficient profiles were retrieved from the ALI data that show reasonable agreement with OSIRIS satellite measurements.

No large scale issues were found with the instrument performance; however, some future changes would be recommended. First, an absolute calibration of the instrument would allow ALI to determine the effect albedo directly, as is done with OSIRIS. This would remove some the uncertainty in the model inputs and likely yield higher quality results. This is simply a matter of having access to the calibration equipment. Also, even with the baffle and the robust method of removing stray light with the cycling of the AOTF, some stray light was still observed in the obtained images. Impact and mitigation of this should be tackled in future iterations of the instrument.

Acknowledgements

This work would have not been possible without funding from the CSA to design and build ALI through the FAST program as well as the CSA building and managing the launch facility

1 in Timmins, Ontario. Also, thanks to CNES for funding and overseeing the launches at Timmins
2 in 2014. The optical design analysis was performed in thanks to Synopsys for the use of a Code
3 V software license. The CALIPSO data were obtained from the NASA Langley Research
4 Center Atmospheric Science Data Center. As well, thanks to Nick Lloyd for help in
5 development of the flight code, without his efforts this work would have not been accomplished.

6 **References**

7 Andersson, S. M., B. G. Martinsson, J.-P. Vernier, J. Friberg, C. A. Brenninkmeijer, M.
8 Hermann, P. F. van Velthoven, and A. Zahn (2015), Significant radiative impact of volcanic
9 aerosol in the lowermost stratosphere, *Nature*, 6.

10 Beuttell, R. G., and A. W. Brewer (1949), Instruments for the measurement of the visual range,
11 *J. Sc. Instrum.*, 26, 357.

12 Bourassa, A. E., D. A. Degenstein, R. L. Gattinger, and E. J. Llewellyn (2007), Stratospheric
13 aerosol retrieval with optical spectrograph and infrared imaging system limb scatter
14 measurements, *J. Geophys. Res.*, 112, D10217, doi:10.1029/2006JD008079.

15 Bourassa, A. E., D. A. Degenstein, and E. J. Llewellyn (2008), SASKTRAN: A spherical
16 geometry radiative transfer code for efficient estimation of limb scattered sunlight, *J. Quant.*
17 *Spectros. and Radia. Transfer*, 109, 52-73, doi:10.1016/j.jqsrt.2007.07.007.

18 Bourassa, A. E., C. A. McLinden, A. F. Bathgate, B. J. Elash, and D. A. Degenstein (2012a),
19 Precision estimate for Odin-OSIRIS limb scatter retrievals, *J. Geophys. Res.*, 117, D04303,
20 doi:10.1029/2011JD016976.

21 Bourassa, A. E., L. A. Rieger, N. D. Lloyd, and D. A. Degenstein (2012b), Odin-OSIRIS
22 stratospheric aerosol data product and SAGE III intercomparison, *Atmospheric Chemistry*
23 *& Physics*, 12, 605-614, doi:10.5194/acp-12-605-2012.

24 Bourassa, A. E., A. Robock, W. J. Randel, T. Deshler, L. A. Rieger, N. D. Lloyd, E. T.
25 Llewellyn, and D. A. Degenstein (2012), Large volcanic aerosol load in the stratosphere
26 linked to Asian monsoon transport, *Science*, 337, 78-81.

27 Bourassa, A. E., A. Robock, W. J. Randel, T. Deshler, L. A. Rieger, N. D. Lloyd, E. Llewellyn,
28 and D. A. Degenstein (2013), Response to comments on "large volcanic aerosol load in the
29 stratosphere linked to Asian monsoon transport", *Science*, 339, 647-647.

- 1 Bovensmann, H., J. Burrows, M. Buchwitz, J. Frerick, S. Noël, V. Rozanov, K. Chance, and A.
2 Goede (1999), SCIAMACHY: Mission objectives and measurement modes, *Journal of the*
3 *Atmospheric Sciences*, 56, 127-150.
- 4 Charlson, R. J., N. Ahlquist, H. Selvidge, and P. MacCready Jr (1969), Monitoring of
5 atmospheric aerosol parameters with the integrating nephelometer, *Journal of the Air*
6 *Pollution Control Association*, 19, 937-942.
- 7 Chazette, P., C. David, J. Lefrere, S. Godin, J. Pelon, and G. Mégie (1995), Comparative lidar
8 study of the optical, geometrical, and dynamical properties of stratospheric postvolcanic
9 aerosols, following the eruptions of el chichon and mount pinatubo, *J. Geophys. Res.*, 100,
10 23-195.
- 11 Cisewski, M., J. Zawodny, J. Gasbarre, R. Eckman, N. Topiwala, O. Rodriguez-Alvarez, D.
12 Cheek, and S. Hall (2014), The stratospheric aerosol and gas experiment (SAGE III) on the
13 international space station (ISS) mission, *Proc. SPIE*, 9241, 924,107-924,107-7,
14 doi:10.1117/12.2073131.
- 15 Clarisse, L., P.-F. Coheur, N. Theys, D. Hurtmans, and C. Clerbaux (2014), The 2011 Nabro
16 eruption, a SO₂ plume height analysis using IASI measurements, *Atmospheric Chemistry*
17 *and Physics*, 14, 3095-3111, doi:10.5194/acp-14-3095-2014.
- 18 Damadeo, R. P., J. M. Zawodny, L. W. Thomason, and N. Iyer (2013), SAGE version 7.0
19 algorithm: application to SAGE II, *Atmos. Meas. Tech.*, 6, 3539-3561, doi:10.5194/amt-6-
20 3539-2013.
- 21 Dee, D. P., S. M. Uppala, A. J. Simmons, P. Berrisford, P. Poli, S. Kobayashi, U. Andrae, M.
22 A. Balmaseda, G. Balsamo, P. Bauer, P. Bechtold, A. C. M. Beljaars, L. van de Berg, J.
23 Bidlot, N. Bormann, C. Delsol, R. Dragani, M. Fuentes, A. J. Geer, L. Haimberger, S. B.
24 Healy, H. Hersbach, E. V. Hlm, L. Isaksen, P. Killberg, M. Khler, M. Matricardi, A. P.
25 McNally, B. M. Monge-Sanz, J.-J. Morcrette, B.-K. Park, C. Peubey, P. de Rosnay, C.
26 Tavolato, J.-N. Thpaut, and F. Vitart (2011), The ERA-interim reanalysis: configuration and
27 performance of the data assimilation system, *Quarterly Journal of the Royal Meteorological*
28 *Society*, 137, 553-597, doi:10.1002/qj.828.
- 29 Dekemper, E., N. Loodts, B. V. Opstal, J. Maes, F. Vanhellemont, N. Mateshvili, G. Franssens,
30 D. Pieroux, C. Bingen, C. Robert, L. D. Vos, L. Aballea, and D. Fussen (2012), Tunable

- 1 acousto-optic spectral imager for atmospheric composition measurements in the visible
- 2 spectral domain, *Applied Optics*, 51, 6259-6267, doi:10.1364/AO.51.006259.
- 3 Deshler, T., M. Hervig, D. Hofmann, J. Rosen, and J. Liley (2003), Thirty years of in situ
- 4 stratospheric aerosol size distribution measurements from Laramie, Wyoming (41 N), using
- 5 balloon-borne instruments, *J. Geophys. Res.*, 108.
- 6 Deshler, T., R. Anderson-Sprecher, H. Jger, J. Barnes, D. J. Hofmann, B. Clemesha, D.
- 7 Simonich, M. Osborn, R. G. Grainger, and S. Godin-Beekmann (2006), Trends in the
- 8 nonvolcanic component of stratospheric aerosol over the period 1971-2004, *J. Geophys.*
- 9 *Res.*111, doi:10.1029/2005JD006089.
- 10 Dueck, S., A. E., Bourassa, and D. A. Degenstein (2015), SASKTRAN-HR Polarization
- 11 Module, In Preparations.
- 12 Ernst, F., C. von Savigny, A. Rozanov, V. Rozanov, K.-U. Eichmann, L. A. Brinkho, H.
- 13 Bovensmann, and J. P. Burrows (2012), Global stratospheric aerosol extinction profile
- 14 retrievals from SCIAMACHY limb-scatter observations, *Atmos. Meas. Tech.*, 5, 5993-6035,
- 15 doi:10.5194/amtd-5-5993-2012.
- 16 Fairlie, T. D., J.-P. Vernier, M. Natarajan, and K. M. Bedka (2014), Dispersion of the Nabro
- 17 volcanic plume and its relation to the Asian summer monsoon, *Atmospheric Chemistry and*
- 18 *Physics*, 14, 7045-7057, doi:10.5194/acp-14-7045-2014.
- 19 Fischer, R. E., B. Tadic-Galeb, and P. R. Yoder (2008), *Optical System Design*, 2nd ed.,
- 20 McGraw-Hill.
- 21 Fromm, M., G. Nedoluha, and Z. Charvt (2013), Comment on "large volcanic aerosol load in
- 22 the stratosphere linked to Asian monsoon transport", *Science*, 339, 647,
- 23 doi:10.1126/science.1228605.
- 24 Fromm, M., G. Kablick, G. Nedoluha, E. Carboni, R. Grainger, J. Campbell, and J. Lewis
- 25 (2014), Correcting the record of volcanic stratospheric aerosol impact: Nabro and sarychev
- 26 peak, *J. Geophys. Res.*, 119, 10,343-10,364, doi:10.1002/2014JD021507.
- 27 Fyfe, J. C., N. P. Gillett, and F. W. Zwiers (2013), Overestimated global warming over the past
- 28 20 years, *Nature Climate Change*, 3, 767-769.

- 1 Georgiev, G., D. A. Glenar, and J. J. Hillman (2002), Spectral characterization of acousto-optic
2 filters used in imaging spectroscopy, *Applied Optics*, 41, 209-217,
3 doi:10.1364/AO.41.000209.
- 4 Gilbert, K., D. Turnbull, K. Walker, C. Boone, S. McLeod, M. Butler, R. Skelton, P. Bernath,
5 F. Chateauneuf, and M.-A. Soucy (2007), The onboard imagers for the Canadian ACE
6 SCISAT-1 mission, *J. Geophys. Res.*, 112.
- 7 Haywood, J. M., A. Jones, and G. S. Jones (2014), The impact of volcanic eruptions in the
8 period 2000-2013 on global mean temperature trends evaluated in the HadGEM2-ES climate
9 model, *Atmospheric Science Letters*, 15, 92-96, doi:10.1002/asl2.471.
- 10 Hofmann, D., J. Barnes, M. O'Neill, M. Trudeau, and R. Neely (2009), Increase in background
11 stratospheric aerosol observed with lidar at Mauna Loa observatory and Boulder, Colorado,
12 *Geophys. Res. Lett.*, 36, doi:10.1029/2009GL039008, 115808.
- 13 Junge, C. E., C. W. Chagnon, and J. E. Manson (1961), Stratospheric Aerosols, *Journal of*
14 *Atmospheric Sciences*, 18, 81-108, doi:10.1175/1520-0469(1961)018h0081:SAi2.0.CO;2.
- 15 Kiehl, J. T., and B. P. Briegleb (1993), The relative roles of sulfate aerosols and greenhouse
16 gases in climate forcing, *Science*, 260, 311-314, doi:10.1126/science.260.5106.311.
- 17 Kosch, M., S. Mäkinen, F. Sigernes, and O. Harang (2003), Absolute optical calibration using
18 a simple tungsten light bulb: Experiment, *Proceedings of the 30th Annual European Meeting*
19 *on Atmospheric Studies by Optical Methods*, 50-54.
- 20 Kovilakam, M., and T. Deshler (2015), On the accuracy of stratospheric aerosol extinction
21 derived from in situ size distribution measurements and surface area density derived from
22 remote SAGE II and HALOE extinction measurements, *J. Geophys. Res.*, 120, 8426-8447,
23 doi:10.1002/2015JD023303, 2015JD023303.
- 24 Llewellyn, E., N. D. Lloyd, D. A. Degenstein, R. L. Gattinger, S. V. Petelina, A. E. Bourassa, J.
25 T. Wiensz, E. V. Ivanov, I. C. McDade, B. H. Solheim, J. C. McConnell, C. S. Haley, C. von
26 Savigny, C. E. Sioris, C. A. McLinden, E. Grifoen, J. Kaminski, W. F. J. Evans, E. Puckrin,
27 K. Strong, V. Wehrle, R. H. Hum, D. J. W. Kendall, J. Matsushita, D. P. Murtagh, S.
28 Brohede, J. Stegman, G. Witt, G. Barnes, W. F. Payne, L. Piche, K. Smith, G. Warshaw, D.
29 L. Deslauniers, P. Marchand, E. H. Richardson, R. A. King, I. Wevers, W. McCreath, E.
30 Kyrola, L. Oikarinen, G. W. Leppelmeier, H. Auvinen, G. Megie, A. Hauchecorne, F.
31 Lefevre, J. de La Noe, P. Ricaud, U. Frisk, F. Sjöberg, F. von Scheele, and L. Nordh (2004),

- 1 The OSIRIS instrument on the Odin spacecraft, *Canadian Journal of Physics*, 82, 411-422,
2 doi:10.1139/p04-005.
- 3 McElroy, C. T., C. R. Nowlan, J. R. Drummond, P. F. Bernath, D. V. Barton, D. G. Dufour, C.
4 Midwinter, R. B. Hall, A. Ogyu, A. Ullberg, D. I. Wardle, J. Kar, J. Zou, F. Nichitiu, C. D.
5 Boone, K. A. Walker, and N. Rowlands (2007), The ACE-MAESTRO instrument on
6 SCISAT: description, performance, and preliminary results, *Applied Optics*, 46, 4341-4356,
7 doi:10.1364/AO.46.004341.
- 8 Murphy, D. M., K. D. Froyd, J. P. Schwarz, and J. C. Wilson (2014), Observations of the
9 chemical composition of stratospheric aerosol particles, *Quarterly Journal of the Royal*
10 *Meteorological Society*, 140, 1269-1278, doi:10.1002/qj.2213.
- 11 Neely, R. R., P. Yu, K. H. Rosenlof, O. B. Toon, J. S. Daniel, S. Solomon, and H. L. Miller
12 (2014), The contribution of anthropogenic SO₂ emissions to the Asian tropopause aerosol
13 layer, *J. Geophys. Res.*, 119, 1571-1579, doi:10.1002/2013JD020578.
- 14 Rault, D. F., and R. P. Loughman (2013), The OMPS limb profiler environmental data record
15 algorithm theoretical basis document and expected performance, *Geoscience and Remote*
16 *Sensing, IEEE Transactions on*, 51, 2505-2527.
- 17 Ridley, D. A., S. Solomon, J. E. Barnes, V. D. Burlakov, T. Deshler, S. I. Dolgii, A. B. Herber,
18 T. Nagai, R. R. Neely, A. V. Nevzorov, C. Ritter, T. Sakai, B. D. Santer, M. Sato, A.
19 Schmidt, O. Uchino, and J. P. Vernier (2014), Total volcanic stratospheric aerosol optical
20 depths and implications for global climate change, *Geophys. Res. Lett.*, 41, 7763-7769,
21 doi:10.1002/2014GL061541, 2014GL061541.
- 22 Rieger, L. A., A. E. Bourassa, and D. A. Degenstein (2014), Stratospheric aerosol particle size
23 information in Odin-OSIRIS limb scatter spectra, *Atmos. Meas. Tech.*, 7, 507-522,
24 doi:10.5194/amt-7-507-2014.
- 25 Rieger, L. A., A. E. Bourassa, and D. A. Degenstein (2015), Merging the OSIRIS and SAGE II
26 stratospheric aerosol records, *J. Geophys. Res.*, doi:10.1002/2015JD023133,
27 2015JD023133.
- 28 Rodgers, C. (2000), *Inverse Methods for Atmospheric Sounding: Theory and Practice*, Series
29 on atmospheric, oceanic and planetary physics: 1999, World Scientific.

- 1 Rogers, R. R., C. A. Hostetler, J. W. Hair, R. A. Ferrare, Z. Liu, M. D. Obland, D. B. Harper,
2 A. L. Cook, K. A. Powell, M. A. Vaughan, and D. M. Winker (2011), Assessment of the
3 CALIPSO lidar 532 nm attenuated backscatter calibration using the NASA LARC airborne
4 high spectral resolution lidar, *Atmospheric Chemistry and Physics*, 11, 1295-1311,
5 doi:10.5194/acp-11-1295-2011.
- 6 Russell, P., and M. McCormick (1989), SAGE II aerosol data validation and initial data use:
7 An introduction and overview, *J. Geophys. Res.*, 94, 8335-8338.
- 8 Sawamura, P., J. P. Vernier, J. E. Barnes, T. A. Berko, E. J. Welton, L. Alados-Arboledas, F.
9 Navas-Guzmn, G. Pappalardo, L. Mona, F. Madonna, D. Lange, M. Sicard, S. Godin-
10 Beekmann, G. Payen, Z. Wang, S. Hu, S. N. Tripathi, C. Cordoba-Jabonero, and R. M. Ho
11 (2012), Stratospheric AOD after the 2011 eruption of Nabro volcano measured by lidars
12 over the northern hemisphere, *Environmental Research Letters*, 7, 034,013.
- 13 Sioris, C. E., C. D. Boone, P. F. Bernath, J. Zou, C. T. McElroy, and C. A. McLinden (2010),
14 Atmospheric chemistry experiment (ACE) observations of aerosol in the upper troposphere
15 and lower stratosphere from the Kasatochi volcanic eruption, *J. Geophys. Res.*, 115,
16 doi:10.1029/2009JD013469, d00L14.
- 17 Smith, W. J. (2000), *Modern Optical Engineering*, New York: McGraw-Hill.
- 18 Solomon, S., J. S. Daniel, R. R. Neely, J.-P. Vernier, E. G. Dutton, and L. W. Thomason (2011),
19 The persistently variable background stratospheric aerosol layer and global climate change,
20 *Science*, 333, 866-870, doi:10.1126/science.1206027.
- 21 Stocker, T. F., D. Qin, G.-K. Plattner, M. M. Tignor, S. K. Allen, J. Boschung, A. Nauels, Y.
22 Xia, V. Bex, and P. M. Midgley (2013), *Climate Change 2013 The Physical Science Basis*.
- 23 Suhre, D. R., L. J. Denes, and N. Gupta (2004), Telecentric confocal optics for aberration
24 correction of acousto-optic tunable filters, *Applied Optics*, 43, 1255-1260,
25 doi:10.1364/AO.43.001255.
- 26 Thomason, L. W., and G. Taha (2003), SAGE III aerosol extinction measurements: Initial
27 results, *Geophys. Res. Lett.*, 30.
- 28 Thomason, L. W., and J.-P. Vernier (2013), Improved SAGE II cloud/aerosol categorization
29 and observations of the Asian tropopause aerosol layer: 1989-2005, *Atmospheric Chemistry*
30 *and Physics*, 13, 4605-4616, doi:10.5194/acp-13-4605-2013.

- 1 Uchida, N. (1971), Optical properties of single-crystal paratellurite (TeO₂), Phys. Rev. B, 4,
2 3736-3745, doi:10.1103/PhysRevB.4.3736.
- 3 Vanhellemont, F., C. Tetard, A. Bourassa, M. Fromm, J. Dodion, D. Fussen, C. Brogniez, D.
4 Degenstein, K. L. Gilbert, D. N. Turnbull, P. Bernath, C. Boone, and K. A. Walker (2008),
5 Aerosol extinction profiles at 525 nm and 1020 nm derived from ACE imager data:
6 comparisons with GOMOS, SAGE II, SAGE III, POAM III, and OSIRIS, Atmospheric
7 Chemistry and Physics, 8, 2027-2037, doi:10.5194/acp-8-2027-2008.
- 8 Vernier, J.-P., L. Thomason, and J. Kar (2011a), CALIPSO detection of an Asian tropopause
9 aerosol layer, Geophys. Res. Lett., 38.
- 10 Vernier, J.-P., L. W. Thomason, J.-P. Pommereau, A. Bourassa, J. Pelon, A. Garnier, A.
11 Hauchecorne, L. Blanot, C. Trepte, D. Degenstein, and F. Vargas (2011b), Major influence
12 of tropical volcanic eruptions on the stratospheric aerosol layer during the last decade,
13 Geophys. Res. Lett., 38, doi:10.1029/2011GL047563, 112807.
- 14 Vernier, J.-P., L. W. Thomason, T. D. Fairlie, P. Minnis, R. Palikonda, and K. M. Bedka (2013),
15 Comment on "Large volcanic aerosol load in the stratosphere linked to Asian monsoon
16 transport", Science, 339, 647, doi:10.1126/science.1227817.
- 17 Voloshinov, V. (1996), Spectral and polarization analysis of optical images by means of
18 acoustooptics, Optics Laser Technology, 28, 119-127, doi:10.1016/0030-3992(95)00079-8.
- 19 Voloshinov, V. B., and J. C. Mosquera (2006), Wide-aperture acousto-optic interaction in
20 birefringent crystals, Optics and Spectroscopy, 101, 635-641,
21 doi:10.1134/S0030400X06100225.
- 22 Voloshinov, V. B., K. B. Yushkov, and B. B. J. Linde (2007), Improvement in performance of
23 a TeO₂ acousto-optic imaging spectrometer, Journal of Optics A: Pure and Applied Optics,
24 9, 341-347, doi:10.1088/1464-4258/9/4/006.
- 25 von Savigny, C., F. Ernst, A. Rozanov, R. Hommel, K.-U. Eichmann, V. Rozanov, J. P.
26 Burrows, and L. W. Thomason (2015), Improved stratospheric aerosol extinction profiles
27 from SCIAMACHY: validation and sample results, Atmos. Meas. Tech., 8, 8353-8383,
28 doi:10.5194/amtd-8-8353-2015.
- 29 Winker, D. M., W. H. Hunt, and M. J. McGill (2007), Initial performance assessment of
30 CALIOP, Geophys. Res. Lett., 34.

- 1 Wiscombe, W. J. (1980), Improved mie scattering algorithms, *Applied optics*, 19, 1505-1509.
- 2 Xu, J., and R. Stroud (1992), *Acousto-optic devices: principles, design, and applications*, vol.
- 3 12, Wiley-Interscience.
- 4 Zawada, D. J., S. R. Dueck, L. A. Rieger, A. E. Bourassa, N. D. Lloyd, and D. A. Degenstein
- 5 (2015), High resolution and Monte Carlo additions to the SASKTRAN radiative transfer
- 6 model, *Atmos. Meas. Tech.*, 8, 3357-3397, doi:10.5194/amtd-8-3357-2015.

7

8

1

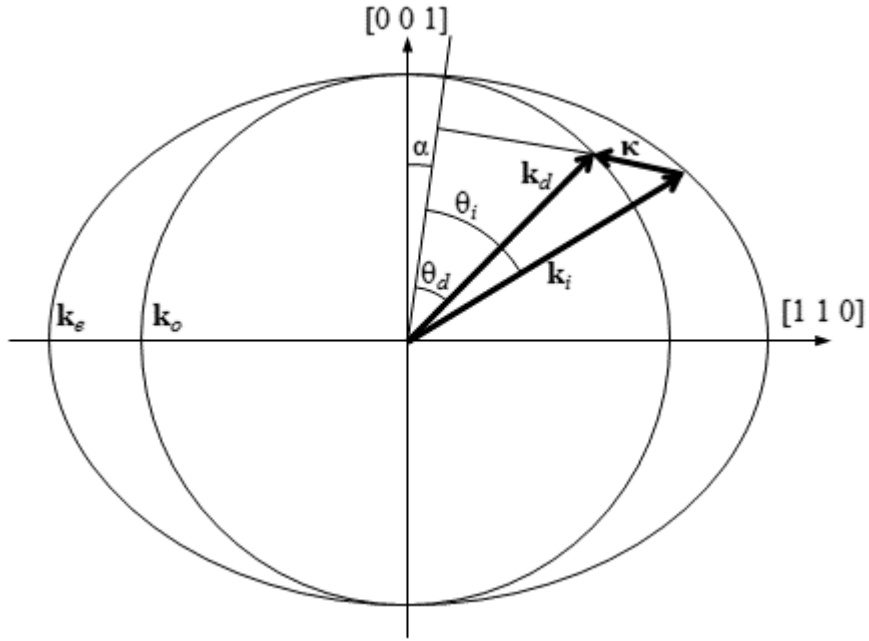
2

Parameter	Value
Effective focal length (mm)	74.3
Front end magnification	0.67
Back end magnification	1.27
Entrance Pupil (mm)	9.91
Field of view (°)	6.0 x 5.0
F-number	7.5
Image size (mm)	9 x 7.5
Image size (pixels)	1000 x 800
Resolved image size (averaged pixels)	143 x 114
Spectral range (nm)	650-950

3

Table 1: ALI final system optical parameters.

1



2 Figure 1: The wave vectors generated by the AOTF experiment. From Equation 1, the incident
 3 wave vector, \mathbf{k}_i , diffracted wave vector, \mathbf{k}_d , and acoustic wave vector $\boldsymbol{\kappa}$ are shown. The
 4 respective interaction angles for the incident and diffracted wave vectors θ_i and θ_d are also
 5 presented.

6

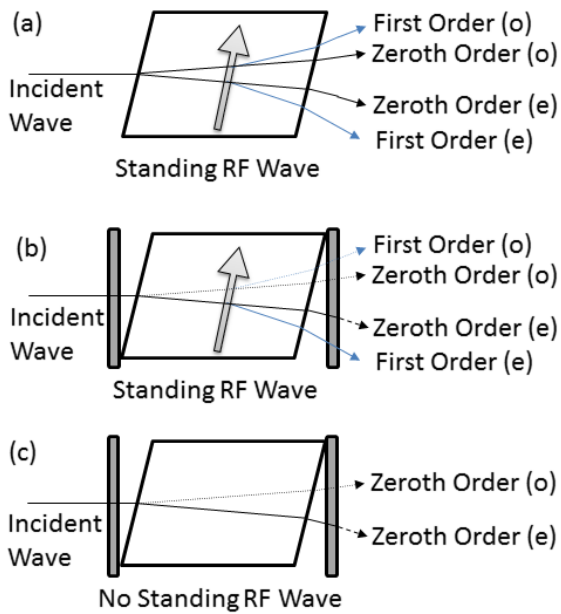


Figure 2: (a) An AOTF undergoing Bragg diffraction with an unpolarised incident wave with a RF wave applied represented by the arrow. After the diffraction event four output signals are formed: the zeroth order and first order ordinary (o) and extraordinary (e) signals. However the only optical path that remains at a constant angle no matter the applied RF wavelength is the first order extraordinary diffracted signal. (b) Two linear polarizers are added to the system, the first linear polarizer removes the ordinary polarization removing the outputs with the dotted lines and the second linear polarizer removes undiffracted extraordinary light shown by the dashed line. (c) The system in (b) without a RF wave so Bragg diffraction is occurring. Once again the first linear polarizer removes the ordinary polarization represented by the dotted line and the second linear polarizer removes the extraordinary light shown by the dashed line.

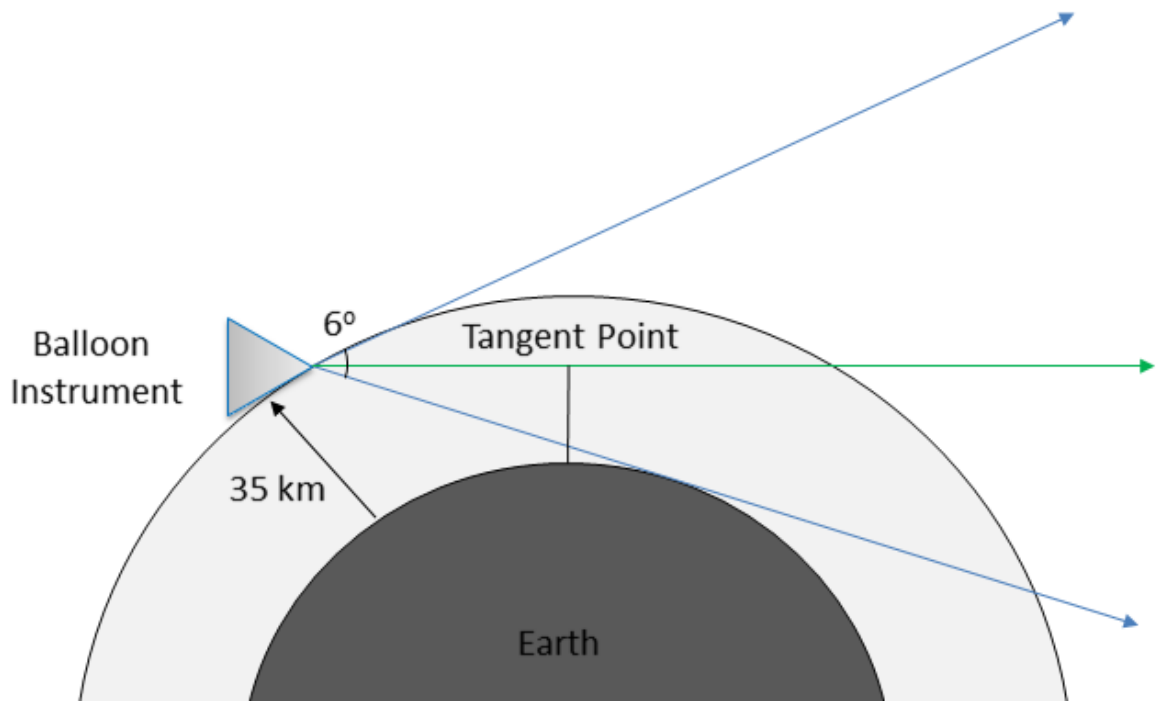


Figure 3: ALI in a stratospheric balloon geometry showing the complete 6° field of view in blue with a float altitude of 35 km. The green line shows a typical vertical line-of-sight where the tangent point or altitude is set by the minimum distance between the earth and the line-of-sight.

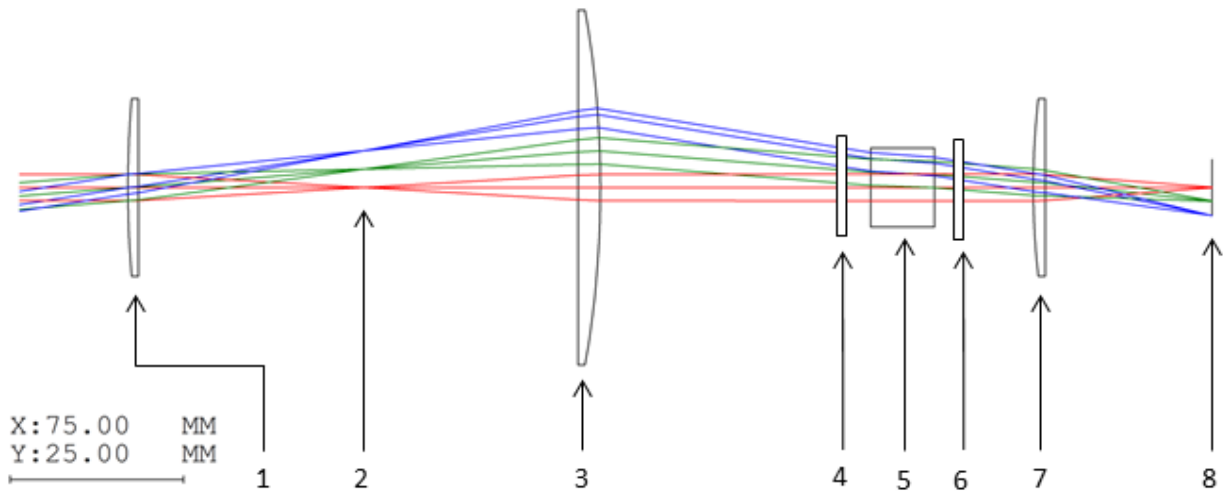
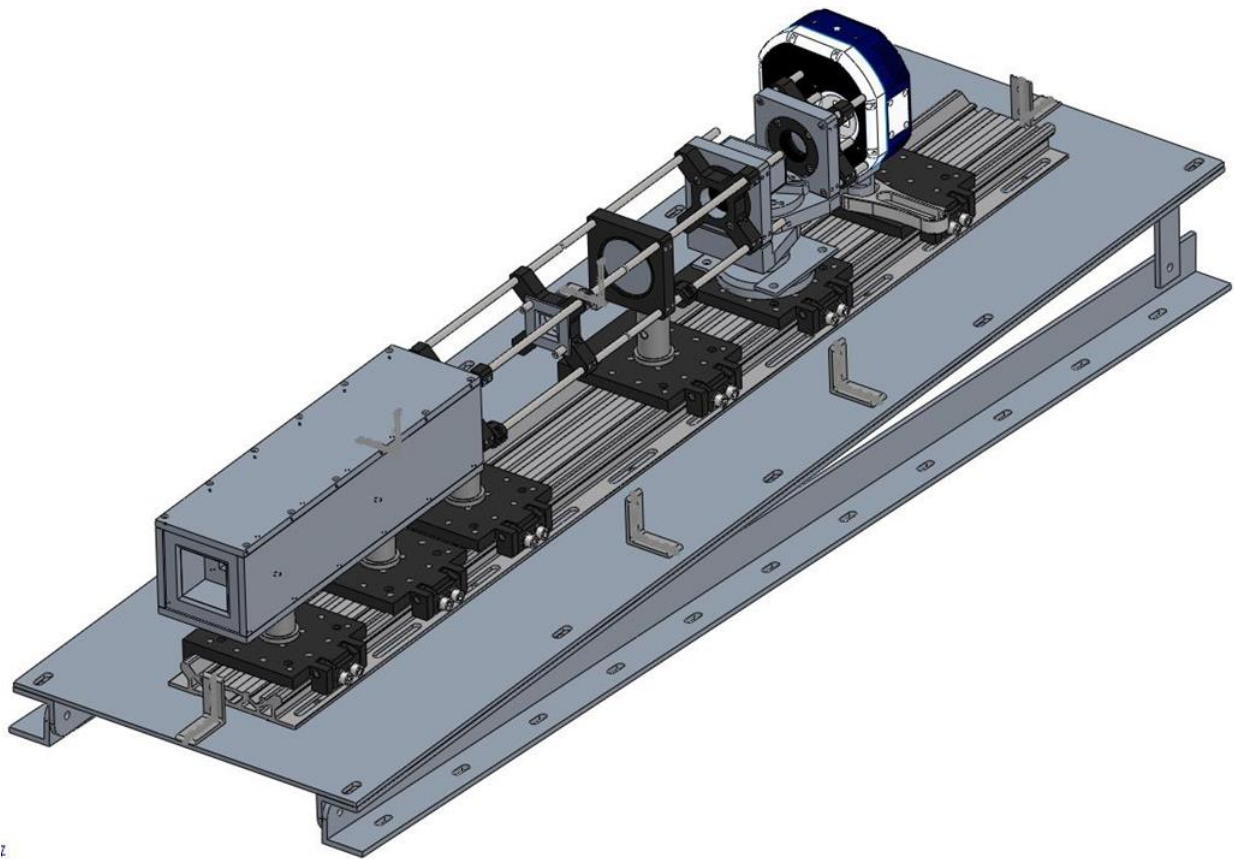
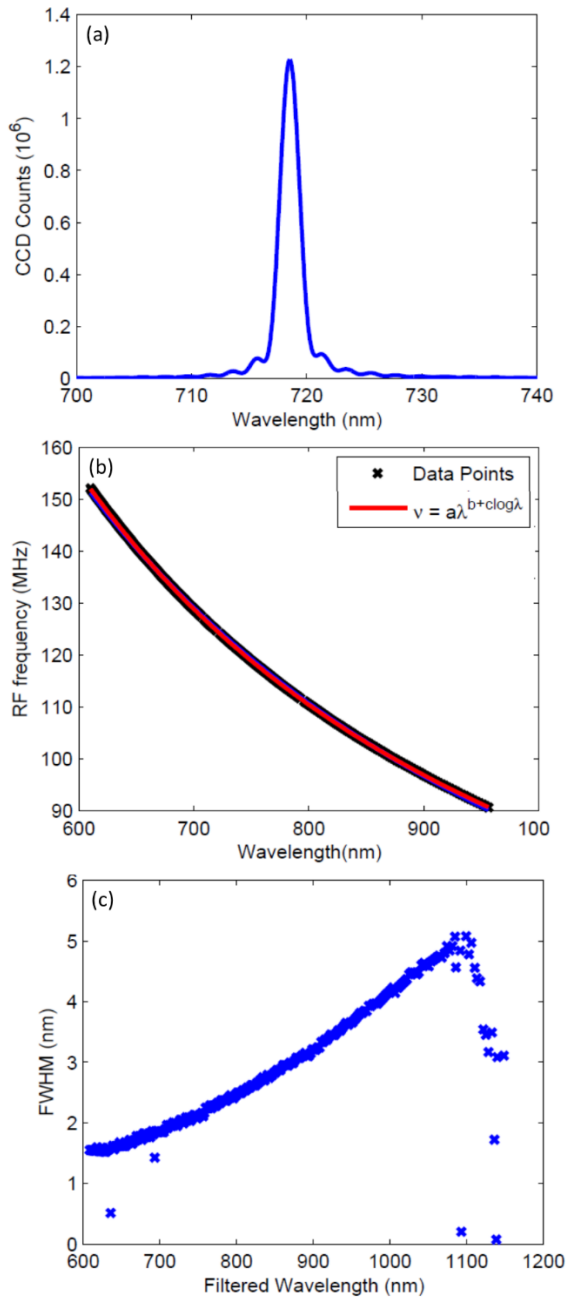


Figure 4: Ray Tracing diagram of the telescopic lens system for ALI simulated by Code V optical design software. The elements in the system are the following: (1) 150 mm focal length plano-convex lens. (2) Field stop. (3) 100 mm focal length plano-convex lens. (4) Vertical linear polarizer. (5) Brimrose AOTF. (6) Horizontal linear polarizer. (7) 50.4 mm focal length bi-convex lens. (8) Imaging plane.



1
2 Figure 5: An isometric view of the complete ALI system with the baffle and 3° slant required
3 to correctly position the field of view. Light tight case absent from diagram.
4



1

2 Figure 6: (a) A spectrum taken from the AOTF from the point spread function when the tuning
3 frequency of the AOTF was at 124.96 MHz. (b) The calibration curves for the AOTF tuning
4 curve which contains the data points recorded and fit curve. (c) The full width half max for each
5 of the determined wavelengths for the AOTF. The full width half max at 600 nm is 1.5 nm and
6 as the wavelengths get longer it increases to 4.9 nm at 1080 nm.

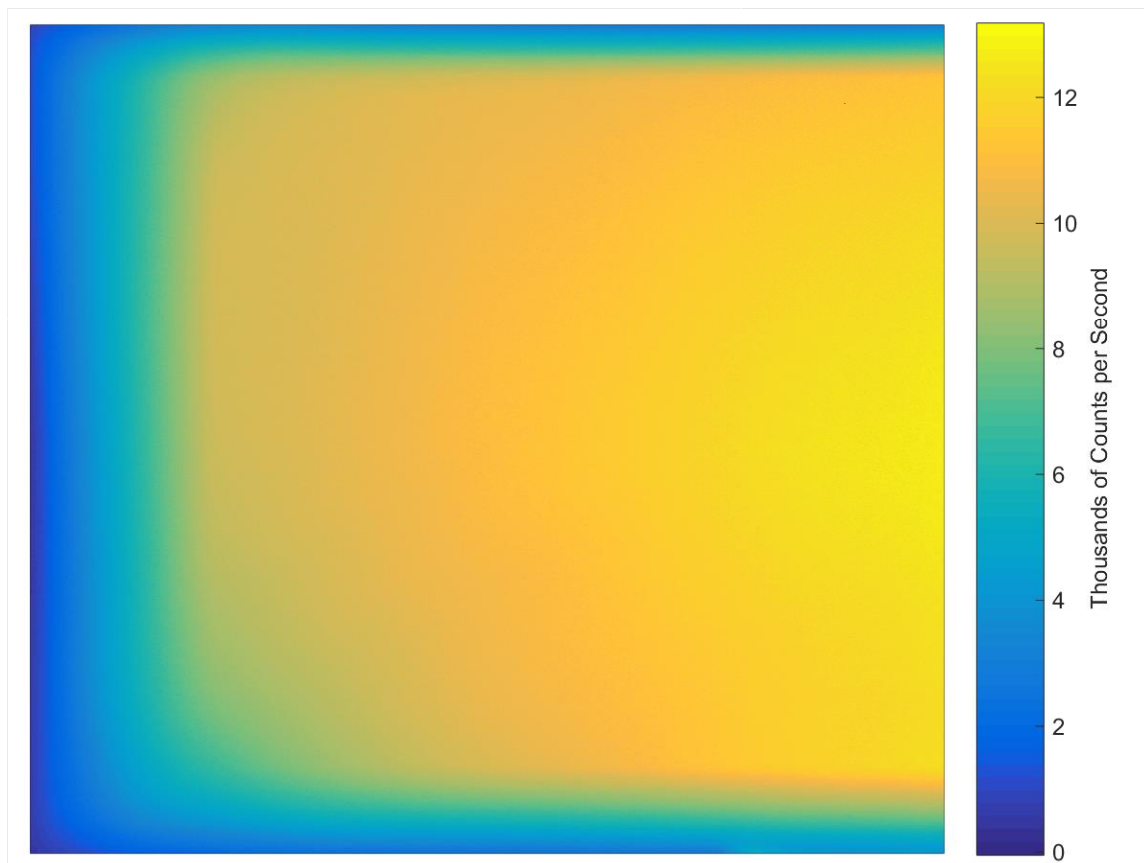


Figure 7: A calibration image after stray light removal has been performed where the measured wavelength is 750 nm with a 1 second exposure time. Vignetting can be seen as moving away from center of the image. Additionally the last 1° of the horizontal field of view on the right side is lost due to strong contamination from reflections within the system.

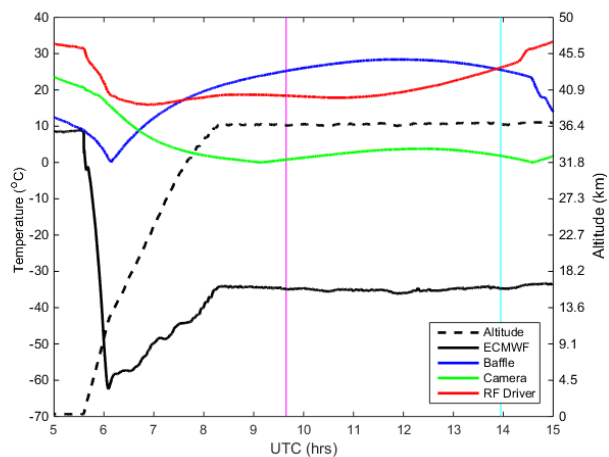
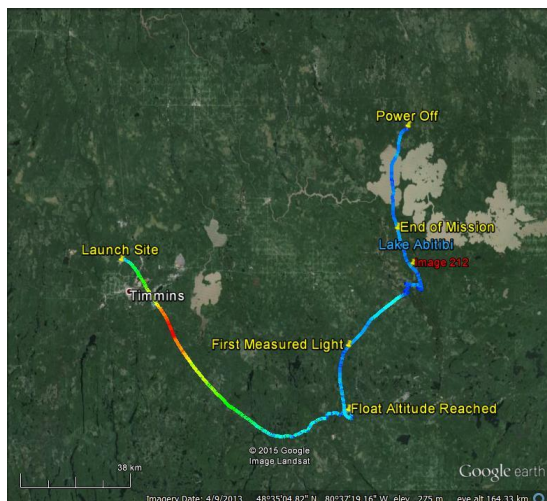


Figure 8: (a) The GPS data from ALI during the Nimbus 7 mission generated via Google Earth. The colour of the line represents the absolute speed of the gondola during the mission. Important landmarks are noted on the image. The end of mission represent the end of the aerosol mission. No GPS data was collected from ALI after power down. The location of image 208 is the red label. (b) The temperature and altitude profiles from the NIMBUS 7 flight. The time of image 208 is shown by the cyan vertical line and first light measured by ALI is occurs at the magenta vertical line.

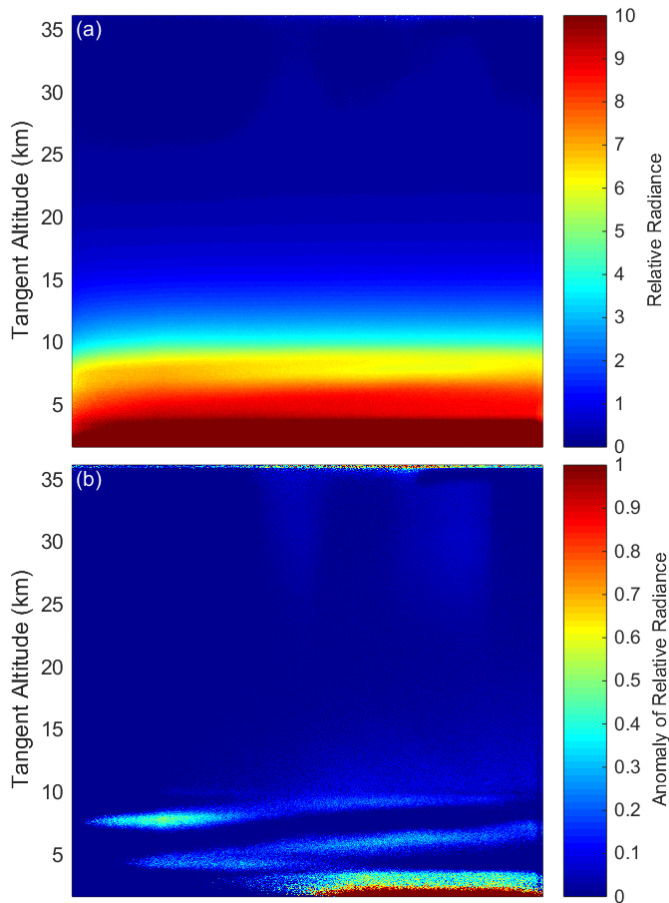


Figure 9: (a) Final calibrated 750 nm image, taken at 13:57 UTC located at 48.55°N, 80.00°W with a solar zenith angle and solar scattering angle of 63° and 98° respectively. (b) The same 750 nm image with the mean of the profile removed from the image leaving the residual signal that shows thin clouds in the troposphere.

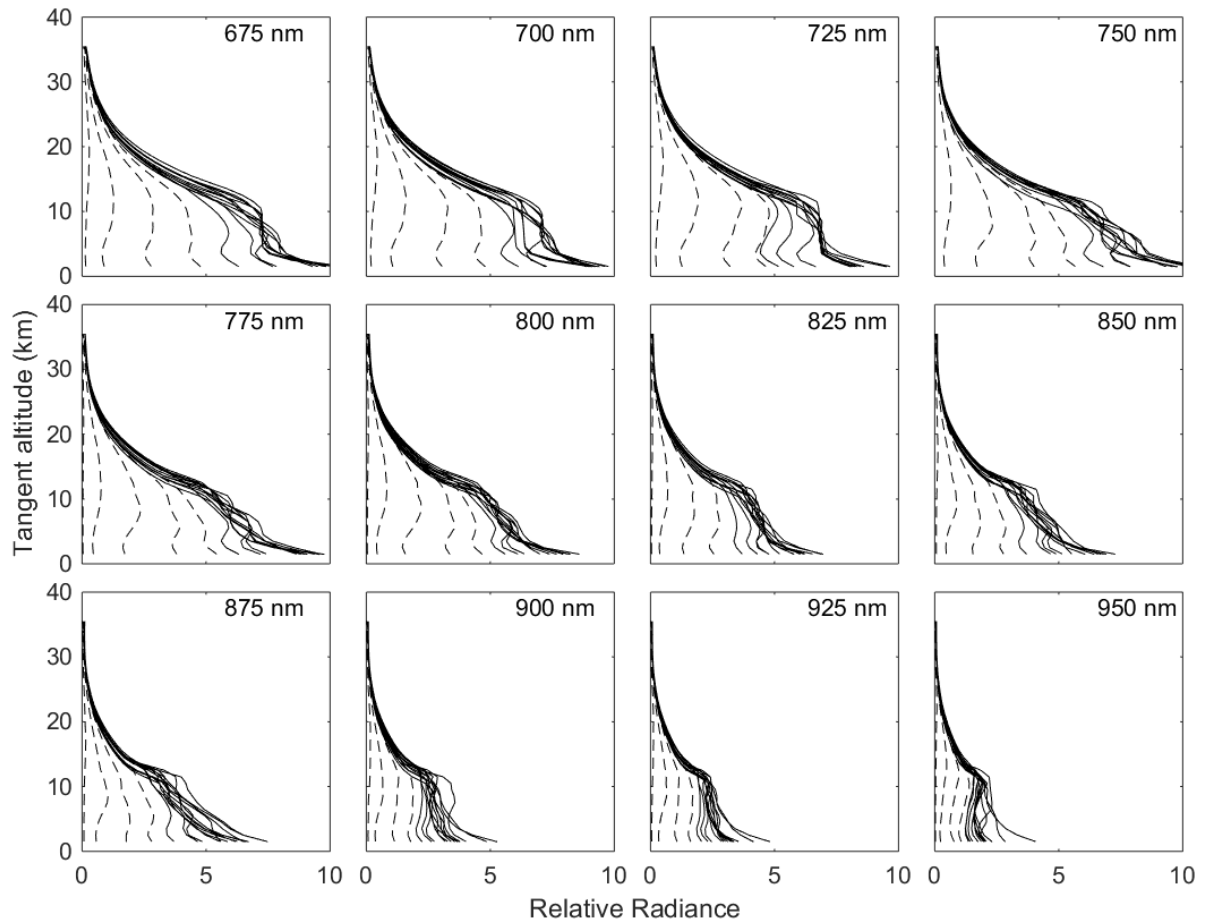


Figure 10: Averaged ALI relative radiance vectors from 12 of the 13 wavelengths from the NIMBUS-7 flight. Each panel presents the radiance vectors from a different wavelength measured which is denoted in the top right corner. The dashed lines are radiance profiles where the solar zenith angle is greater than 90° and solid lines are profile where the solar zenith angle is less than 90° .

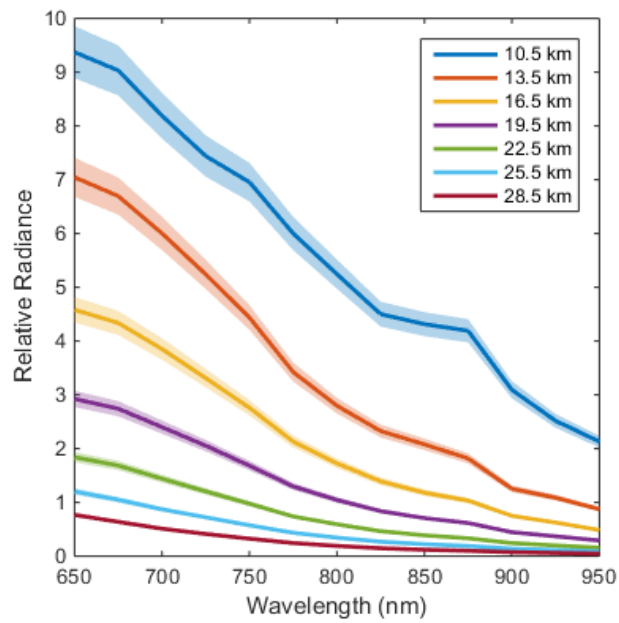


Figure 11: Level 1 relative radiances spectrally from 650 nm to 950 nm as measured from ALI at approximately 14:20 UTC consisting of images number 204 to 216 looking 90° in the azimuth from the sun facing southwards. These spectral profiles are presented at several tangent altitudes with a horizontal look direction of 0°. The shading represents the error on the radiances.

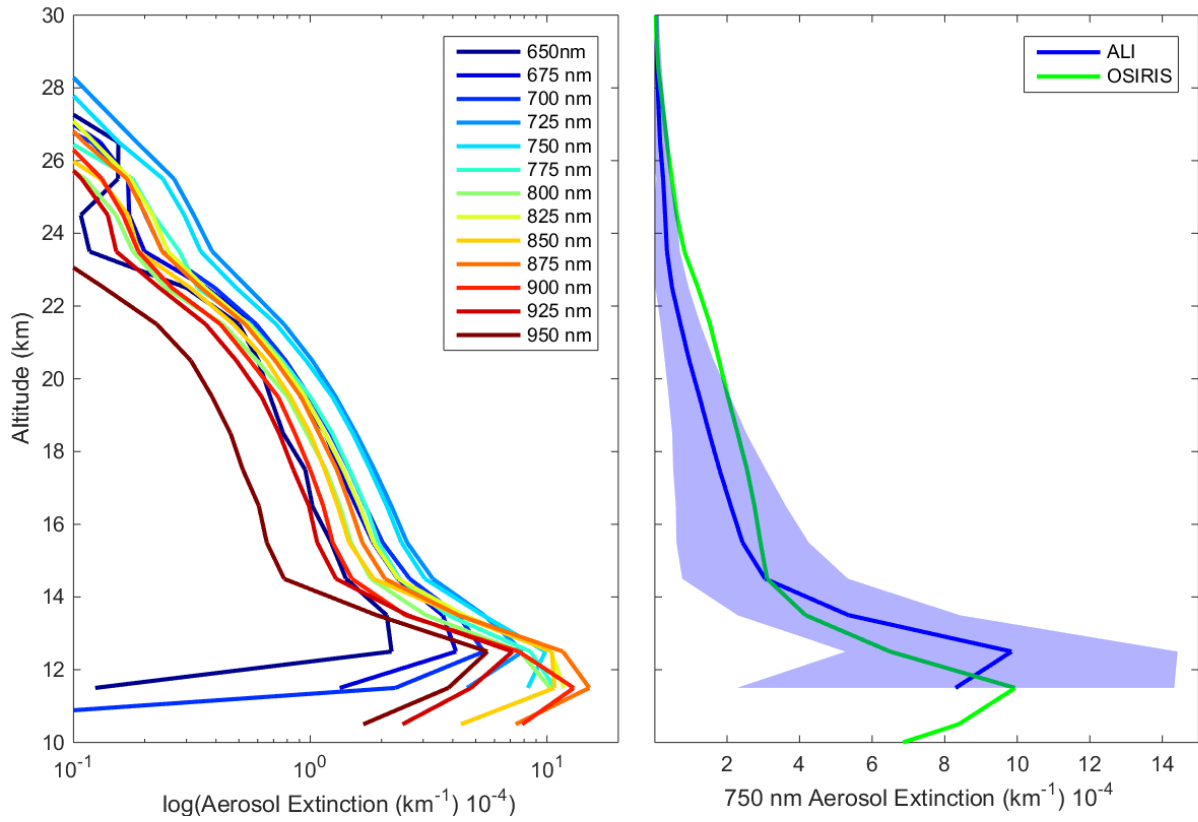


Figure 12: Left is the retrieved aerosol extinction profiles from the last complete imaging cycle consisting of images 205 to 216 from the 0.0° horizontal line-of-sight. Right is the 750 nm ALI aerosol extinction in blue with its error represented by the shading compared to the 750 nm extinction measured by OSIRIS in green.

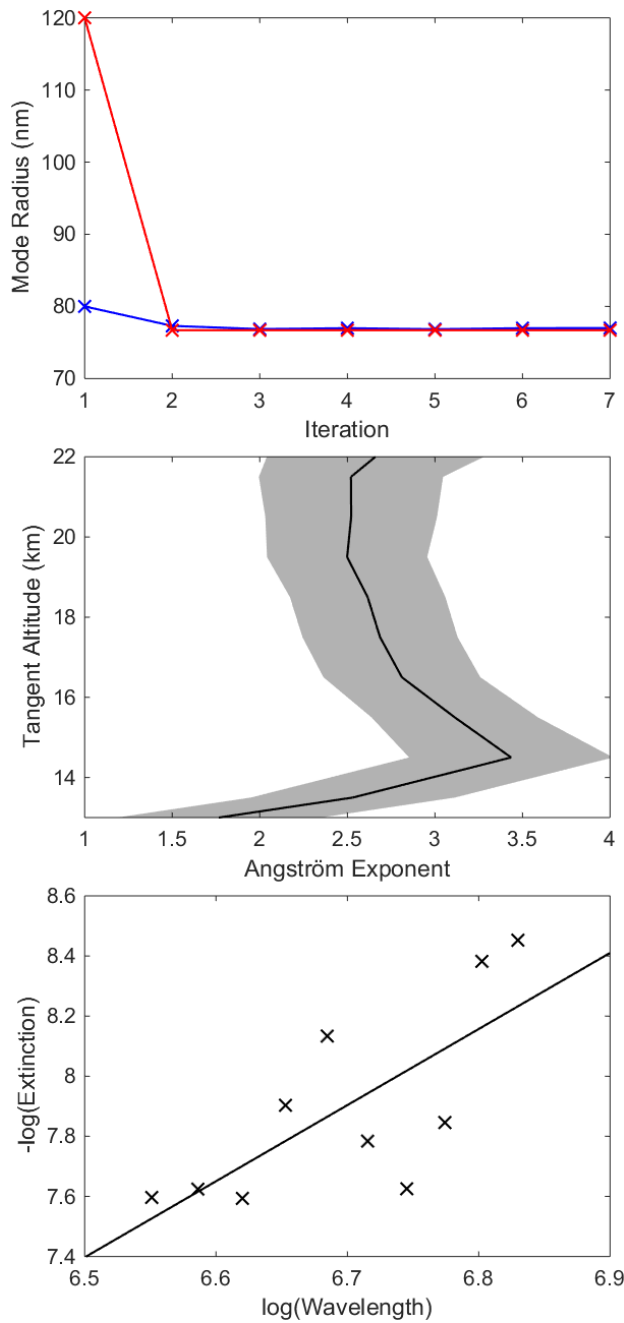


Figure 13: The top panel shows the convergence of two sample particle size retrievals, blue and red represent an initial state of 0.08 and 0.12 μm mode radius respectively. Both initial states converge to the same value over approximately 3 iterations in the particle size retrieval method. The middle panel shows the final Angström exponents determined from images 204-216. The shading represents the error associated with the least squares fit. The bottom panel shows a typical least squares fit of the retrieved extinction values over wavelength to determine the Angström exponent at model altitude of 14.5 km.